CRYSTAL GROWTH & DESIGN

pubs.acs.org/crystal

Article

Crystallization-Induced Deracemization: Experiments and Modeling

Brigitta Bodák,[†] Francesca Breveglieri,[†] and Marco Mazzotti*

Cite This: *Cryst. Growth Des.* 2022, 22, 1427−1436

Read Online

ACCESS | Metrics & More | Article Recommendations

ABSTRACT: Inspired by deracemization via temperature cycles, which enables the collection of crystals of the desired enantiomer from an initially racemic mixture, we focus in this work on an alternative batch process, namely crystallization-induced deracemization. This process starts with a suspension of enantiomerically pure crystals, which undergoes a simple cooling crystallization, coupled with liquid-phase racemization. The experimental and model-based analysis of such a process, carried out here, revealed that: (i) deracemization via temperature cycles is a safe choice to operate with high enantiomeric purity, although its throughput is limited by the suspension density; (ii) if the distomer is less prone to nucleation, crystallization-induced deracemization is a simple process; however, its performance is strongly limited by the solubility; (iii) the purity achieved with crystallization-induced deracemization can be increased by utilizing large seed mass and by optimizing the cooling profile or catalyst concentration. Alternatively, the purity increases via partial dissolution of the seeds, which resembles the heating part of the deracemization process via temperature cycles.

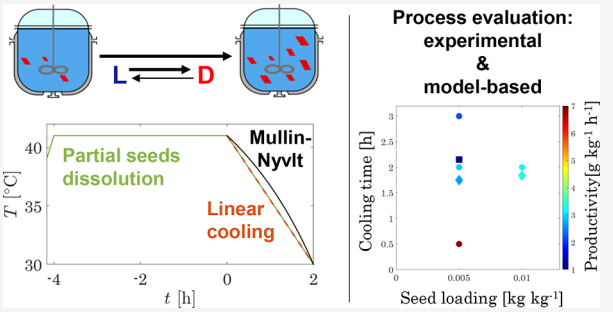

1. INTRODUCTION

Solid-state deracemization processes are particularly appealing, thanks to the combination of crystallization and racemization, which enables the conversion of a suspension consisting of crystals of both enantiomers into an enantiomerically pure crystal suspension. Among these processes,[1−8] deracemization via temperature cycles has been the focus of experimental and modeling studies carried out by various research groups with the aim of identifying the relevant operating parameters and simplifying the process design.[5,9−20] In our recent work,[21] we identified a design parameter, i.e. the dissolution factor, demonstrated its primary role, and showed that high productivity values are attained for small values of the dissolution factor.

These findings motivated us to consider a simpler batch process, whereby the initial suspension, consisting of pure crystals of the target enantiomer ($ee_0 = 1$) in a racemic solution, is cooled from an initial to a final temperature; the presence of a racemizing agent hinders the nucleation of crystals of the distomer by enabling its conversion into the eutomer. We call such a process "crystallization-induced deracemization"; it can be viewed as a limiting case of deracemization via temperature cycles, whereby the dissolution steps are spared, as distomer crystals are not present when cooling starts. The conceptual differences are that deracemization via temperature cycles has identical initial and final temperatures, as the aim is the conversion of distomer crystals into eutomer crystals. Thus, the potential nucleation of distomer crystals does not affect the final product purity, while crystallization-induced deracemization begins at high temperature, and being a cooling crystallization, the desired enantiomer is crystallized out of the solution, but the undesired one could also nucleate, thus decreasing the purity of the final product. Therefore, the throughput of the first technique is limited by the suspension density, while the throughput of the second process is limited by the solubility.

The crystallization-induced deracemization (CID) method had already been proposed as a modification of the preferential crystallization process in the literature, where it was called various names: for example, crystallization-induced asymmetric transformation (CIAT)[22] or second-order asymmetric transformation (SOAT).[17,23−25] These earlier works showed that, by application of the appropriate temperature profile, this simple technique enabled the collection of a pure product with higher productivity in comparison to deracemization via temperature cycles.[17,25] However, a systematic analysis of the effect of the operating conditions, which aims at understanding how to tune them to target high purity and productivity, is still lacking.

In this work, first, we present the process design approach, the metrics to evaluate the process performance, and the tools

Received: November 23, 2021
Revised: December 21, 2021
Published: January 6, 2022

https://doi.org/10.1021/acs.cgd.1c01374
Cryst. Growth Des. 2022, 22, 1427−1436

utilized for the analysis. Then, we investigate in modeling (section 4) and experimental studies (section 5) the effect of the process operating parameters on this technique, thus providing the basis for the design of an efficient and productive CID process, as well as for its comparison with the temperature cycle approach.[26]

2. PROCESS DESIGN, MODELING, AND ASSESSMENT CRITERIA

Operating a cooling process requires choosing the initial and final temperatures, seed loading, cooling time, and a specific cooling profile. A simple linear cooling profile may lead to supersaturation levels of the distomer that trigger its nucleation and the loss of enantiopurity. To avoid this, we have developed an alternative nonlinear cooling profile. It is inspired by the classical cooling strategy proposed by Mullin and Nyvlt for seeded cooling crystallization[27] and is based only on the knowledge of solubility: i.e., often the only property known at the time of process design. In the following, we will evaluate the effect of operating conditions on the process performance via both simulations and experiments. Ultimately, we will provide a clear strategy on how to operate the CID process so as to exploit its advantageous characteristics and to avoid its more critical aspects.

2.1. Mullin–Nyvlt-Based Trajectory for Crystallization-Induced Deracemization. We propose an alternative temperature trajectory that can be easily implemented in a batch seeded crystallization process, when only the solubility of the compound of interest is known. This approach is based on that proposed by Mullin and Nyvlt, where the concentration and the corresponding temperature trajectory result in the growth of a single population of crystals at a constant rate, while nucleation is avoided.[27] In this work, we propose the Mullin–Nyvlt-based trajectory for batch CID of two populations of enantiopure crystals, whereby we make the additional assumption of equal concentrations of the two enantiomers in solution, i.e. of instantaneous racemization, which is obviously a reasonable assumption when racemization is fast enough. For the detailed derivation of the Mullin–Nyvlt based trajectory for deracemization, which follows the dimensionless framework proposed by Ward et al.,[28] the reader is referred to Appendix C.

The calculation of this temperature profile depends only on the solubility of the pure enantiomer that we assume to be given by the exponential function $c^*(T) = q_0 \exp(-q_1/T)$ and on the process operating conditions; no information about the kinetics of the process is required. The evolution of the temperature over time is obtained as a function of the initial and final racemate concentrations, c_0^{tot} and c_{final}^{tot}, respectively, of the mass of seeds per unit mass of solvent, m_s, and of the cooling time, t_{cool}, and it is given by the expression

$$T(\tau) = -q_1\left[\log\left(c_{final}^{tot} + (c_0^{tot} - c_{final}^{tot})\left(1 - \frac{(1+\alpha\tau)^3 - 1}{(1+\alpha)^3 - 1}\right)\right) - \log 2q_0\right]^{-1} \quad (1)$$

where α is defined as $\alpha = (1/\mu_s + 1)^{1/3} - 1$, $\mu_s = m_s/(c_0^{tot} - c_{final}^{tot})$ is the dimensionless seed mass, and $\tau = t/t_{cool}$ is the dimensionless time.

We remark in passing that another nonlinear cooling profile, different from that proposed here, was investigated in the literature to improving the performance of the CID process: more specifically, a cubic trajectory.[25] Such a trajectory was proposed by Mullin for cooling crystallization assuming a constant rate of growth in the absence of nucleation and under the condition that the temperature derivative of solubility is not temperature dependent: i.e. assuming the solubility is a linear funtion of temperature[29] (note that in this work, we use the exponential dependence of solubility on temperature).

2.2. Performance Assessment. The evaluation of the process performance is based on the productivity, product purity, and yield.

2.2.1. Productivity. This key performance indicator (KPI) is defined as (see eq 13 in a previous work[15])

$$P = \frac{k_v \rho_c}{t_{process}}[(\phi_{3,final}^{D} - \phi_{3,final}^{L}) - (\phi_{3,0}^{D} - \phi_{3,0}^{L})] \quad (2)$$

where ϕ_3^D is the third moment of the PSD, proportional to the crystal mass, of the desired enantiomer, ϕ_3^L is that of the undesired enantiomer, at the beginning and at the end of the process, labeled with the subscripts "0" and "final", respectively, and $t_{process}$ is given by the time between the seeding and the end of the cooling ramp. We remark that the cooling time, t_{cool}, is also used in this study to comparatively assess the effect of various temperature profiles, but the KPIs are computed in all cases utilizing $t_{process}$, which can include additional heating/isothermal phases. Note that to obtain the productivity values with the desired units, i.e. g kg^{-1} h^{-1}, one needs to convert the model output accordingly. In the experiments, the initial and final amounts of the eutomer are obtained from the ee and the total masses of the solid at the beginning and the end of the cooling phase. The latter is computed by adding to the amount seeded initially the difference between the solution concentration before and after cooling, as measured gravimetrically.

2.2.2. Purity. The experimental product purity is given by the final enantiomeric excess ee_{final}, obtained from the HPLC analysis of the final solid. Since the process model does not account for nucleation of the distomer and the process is started with the assumption of ideally enantiomerically pure seed crystals ($\phi_{3,0}^L$ and $\phi_{3,final}^L$ are 0), in simulations the final ee is always 1. Therefore, the maximum supersaturation of the distomer reached during the process, S_{max}^L, is used as an indication of the product purity: the larger the S_{max}^L, the higher the risk of triggering nucleation and hence the lower the product purity.

2.2.3. Yield. The yield is computed by subtracting the mass of seed crystals at the beginning of the process from the mass of product crystals (Gou et al.[30])

$$Y = \frac{m_{final} - m_0}{m_{liq,0}^{D}}\ [-] \quad (3)$$

where $m_{liq,0}^D$ is the mass of the desired enantiomer in the solution at the beginning of the process. It is worth noting that the maximum achievable yield is larger than one due to the conversion of the distomer (L enantiomer) into the eutomer (D enantiomer) by racemization.

2.3. Process Modeling. The population balance equation (PBE) based model, developed earlier in our group with the primary aim of simulating deracemization via temperature cycles, has been utilized to simulate crystallization-induced deracemization. The model receives as an input a given

https://doi.org/10.1021/acs.cgd.1c01374
Cryst. Growth Des. 2022, 22, 1427−1436

temperature profile, which in the case of temperature cycles is a periodic oscillation and in the case of crystallization-induced deracemization is a cooling profile, as specified later. The model requires the initial particle size distribution for each enantiomer, f_0^i; for the distomer this is obviously 0, while for the eutomer this is a truncated Gaussian distribution, symmetric about its mean (the rescaled parameters of f_0^D are $\lambda_{1,0,i}^0$ and $\tilde{\sigma}_i^0$, see Table 2). As the model has been discussed in depth in previous works,[10,15,31] in this work, we summarize only the dimensional equations in Table 1. The values of the model parameters that were kept constant during the simulations are reported in Table 2, while the parameters varied in the simulations study are reported in Table 3. Thanks to the versatility of our modeling platform, we were able to simulate CID by setting the temperature profile to the desired cooling profiles: namely, the (i) linear cooling profile (LIN) and (ii) the Mullin−Nyvlt-based profile for deracemization (M-N, section 2.1).

Table 1. System of Equations That Form the Basis of the PBE Model[a]

$$\frac{\partial f^i}{\partial t} + \frac{\partial (G^i(S_\infty^i, T, L) f^i)}{\partial L} = 0 \quad (4)$$

$$\frac{\mathrm{d}c^i}{\mathrm{d}t} + k_v \rho_c \frac{\mathrm{d}\phi_3^i}{\mathrm{d}t} = R^i(c^i, c^j, T) \quad (5)$$

$$f^i(L, 0) = f_0^i(L) \quad (6)$$

$$f^i(0, t) = 0 \quad (7)$$

$$c^i(0) = c_\infty(0) \quad (8)$$

$$\phi_n^i(t) = \int_0^{+\infty} L^n f^i(L, t)\, \mathrm{d}L \quad (9)$$

$$c_\infty(T) = q_0 \exp\left(-\frac{q_1}{T}\right) \quad (10)$$

$$G^i(S_\infty^i, T, L) = \begin{cases} A_g(T)\sigma^i(S_\infty^i, T, L), \sigma^i(S_\infty^i, T, L) > 0 \\ A_d(T)\sigma^i(S_\infty^i, T, L), \sigma^i(S_\infty^i, T, L) \le 0 \end{cases} \quad (11)$$

$$\text{with } \sigma^i(S_\infty^i, T, L) = \left(S_\infty^i - 1 - \frac{\alpha_0}{LT}\right) \quad S_\infty^i(c^i, T) = \frac{c^i}{c_\infty^i} \quad (12)$$

$$\text{and } A_g(T) = k_g \exp\left(-\frac{E_g}{RT}\right) \quad (13)$$

$$\text{and } A_d(T) = k_d \exp\left(-\frac{E_d}{RT}\right) \quad (14)$$

$$R^i(c^i, c^j, T) = k_{r0} \exp\left(-\frac{E_r}{RT}\right)(c^j - c^i) \quad i, j \in \{\mathrm{D}, \mathrm{L}\} \quad (15)$$

[a]The equations are population balance eq 4, mass balances (eq 5), initial and boundary conditions (eqs 6−8), the moments of the distributions (eq 9), the macroscopic solubility (eq 10), growth and dissolution rates eqs 11−14), and racemization rate eq 15. Nomenclature: f, particle size distribution (PSD); L, particle size; G, growth/dissolution rate; c, concentration; T, temperature; ϕ_n, nth moment of the PSD. The constant parameters and their corresponding values are reported in Appendix A.

3. EXPERIMENTAL METHODS

3.1. Materials. The experiments presented in this work were performed with *N*-(2-methylbenzylidene)-phenylglycine amide (NMPA), which was already used as a model compound in previous works[11,16,21] and was synthesized in our laboratory according to the procedure reported in the literature.[6] This compound is an imine derivative of phenylglycine that racemizes in solution in the presence of the base 1,8-diazabicyclo[5.4.0]undec-7-ene (DBU) as a racemizing agent. As a solvent, a 95 wt % mixture of 2-propanol (IPA) in acetonitrile (ACN) was used. The racemizing agent and the solvents were purchased from Sigma-Aldrich.

Table 2. Values of the Model Parameters[a,10,15]

parameter	notation	value
activation energy of dissolution	E_d (kJ kmol^{-1})	12000
activation energy of growth	E_g (kJ kmol^{-1})	12000
activation energy of racemization	E_r (kJ kmol^{-1})	75000
pre-exponential factor of dissolution	k_d (μm s^{-1})	200
pre-exponential factor of growth	k_g (μm s^{-1})	100
pre-exponential factor of racemization	k_{r0} (s^{-1})	10^{11} (A), 10^{12} (B), ∞ (C)
surface shape factor	k_s (−)	π
volume shape factor	k_v (−)	$\pi/6$
universal gas constant	R (kJ kmol^{-1} K^{-1})	8.314
solubility parameter	q_0 (g g^{-1})	400 (A, C), 3.05 (B)
solubility parameter	q_1 (K)	2500 (A, C), 1075 (B)
capillary length constant	α_0 (K m)	9.2×10^{-7}
crystal density	ρ_c (kg m^{-3})	1300
solvent density	$\rho_{solvent}$ (kg m^{-3})	786
reference size	L_r (μ)	100
reference time	t_r* (s)	$=t_{process}$
minimum temperature	T_{min} (K)	298
reference temperature	T_r (K)	273
rescaled mean size of PSD	$\lambda_{1,0,i}^0$	1
rescaled standard deviation of PSD	$\tilde{\sigma}_i^0$	0.05

[a]Some system parameters are varied on the basis of the compound simulated, which is indicated in parentheses. An asterisk indicates that this parameter varies depending on the process time of each simulation.

Table 3. Parameters Varied in "Crystallization-Induced Deracemization" Simulations[a]

simulation	compound	TP	ΔT (K)	$t_{process}$ (h)	ρ_0 (kg kg^{-1})
1	A	LIN	1−30	0.5−3.0	0.040
2	A	LIN	10	0.2−3.0	0.001−0.100
3	B, C	LIN, M-N	10	0.2−3.0	0.005

[a]In all cases, the minimum temperature was set to T_{min} = 298 K. TP denotes the temperature profile.

3.2. Experimental Protocols. CID experiments were carried out in a 100 mL temperature-controlled EasyMax reactor (Mettler Toledo). Additionally, deracemization via temperature cycle experiments at this process scale and under the given operating conditions were repeated three times as a base for comparison.

In both cases, a solution of NMPA in 50 mL of the solvent mixture IPA/ACN (95/5) in the presence of DBU was stirred overnight (down-pumping 45° pitched blade turbine impeller at 400 rpm) at the desired temperature to allow reaching the thermodynamic equilibrium. The filtered saturated solution at the given initial temperature was then seeded with a specific amount and type of solid; then the specified temperature profile was started. During the process, the solid-phase ee was monitored by sampling 2 × 0.2 mL of the suspension, which was then vacuum-filtered on a Büchner funnel and an MS PTFE 0.5 μm membrane filter and washed with *tert*-butyl methyl ether. The dry samples were then dissolved and analyzed via HPLC according to the protocol described previously.[16] For the CID process, the concentration was measured gravimetrically at chosen

https://doi.org/10.1021/acs.cgd.1c01374
Cryst. Growth Des. 2022, 22, 1427−1436

process times to compute the process productivity. To do that, a sample of the suspension was withdrawn with a syringe, and the solid was removed by means of a syringe filter. The liquid phase was collected in tared vials, which were weighed before and after the solvent evaporation to determine the solution concentration.

Depending on the type of experiment, different seeds and temperature profiles were used.

(1) In deracemization via temperature cycles, a desired amount of enantiomerically enriched solid was suspended in a solution saturated at 30 °C and the usual four-step temperature profile started. This was repeated until an enantiomeric excess (ee) of 0.95 was reached. For the details of this method, we refer the reader to previous papers.[11,16,18]

(2) Crystallization-induced deracemization consists of a seeded cooling crystallization process with racemization in solution. Therefore, the seeds are pure crystals of the desired enantiomer, with ee ≥ 0.96, obtained directly from deracemization via temperature cycles, and the temperature profile (TP) consists essentially of a cooling phase, that can be (1) a simple linear cooling ramp, starting at the saturation temperature, 41 °C, and reaching a temperature of 30 °C with various cooling rates (Figure 1 dashed orange line), (2) the Mullin−Nyvlt-based profile (M-N) introduced in section 2.1, applied between 41 and 30 °C, for the desired seed loading, cooling time, and solubility parameters of NMPA (i.e. q_0 = 332 kg kg^{-1} and q_1 = 3210 K; Figure 1 black line), and (3) alternatively, partial dissolution of the seeds being performed by heating a suspension saturated at 39 to 41 °C in 10 min, and waiting for 4 h to reach equilibrium, before starting to cool linearly down to 30 °C (Figure 1 green line). In this case, the amount of seeds added was 0.007 kg kg^{-1} and corresponded to the amount needed to start the cooling phase with the specified suspension density (ρ_0 = 0.005 kg kg^{-1}).

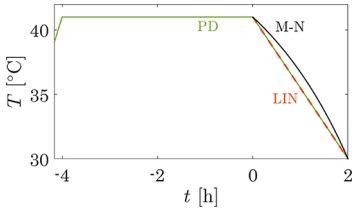

Figure 1. Temperature profile applied in experiments: linear (black dashed line) and Mullin−Nyvlt-based (orange line) cooling profile with $t_{process}$ = 2 h and ρ_0 = 0.01, and temperature profile for partial seed dissolution (green line).

4. SIMULATION STUDY

Through simulations, we have analyzed for the first time the effect of the operating conditions, namely the process time (which obviously corresponds to various cooling rates), the operating temperature range, and the initial suspension density (i.e., the seed mass), on the performance of the crystallization-induced deracemization process on the so-called compound A. The simulation conditions are given in Table 3 and the parameters in Table 2, where the corresponding compound is indicated in parentheses. We remark that, in these simulations, the process time always corresponds to the cooling time, as neither isothermal nor heating phases were implemented.

After commenting on the trends obtained with the linear cooling profile when the temperature variation, ΔT, the process time, $t_{process}$, and the suspension density, ρ_0, vary (LIN in Table 3, simulations 1 and 2), we show how to overcome its limitations by utilizing the Mullin−Nyvlt-based cooling profile (M-N in Table 3). We have compared the performance of the two cooling profiles for two additional simulated compounds: compound B, which has a solubility curve with a weak temperature dependence, and compound C, which has infinitely fast racemization kinetics and hence the two enantiomers in the liquid phase are in equilibrium and at the same concentration (simulation 3; see Table 2 for the values of the model parameters).

4.1. Linear Cooling Profile. The process time, $t_{process}$, the amplitude of the operating temperature range, ΔT, and the initial suspension density, ρ_0, have been varied, thus exploring a three-dimensional parameter space with $t_{process}$, ΔT, and ρ_0 as coordinates. We analyze how productivity (purple contour lines), yield (green contour lines), and maximum supersaturation of the distomer (orange contour lines) vary either as a function of $t_{process}$ and ΔT in Figure 2 (top row; for ρ_0 = 0.040 kg kg^{-1}, simulation 1 in Table 3) or as a function of $t_{process}$ and ρ_0 in Figure 2 (bottom row; at ΔT = 10 K, simulation 2). Note that the final temperature of the process was set to be identical (T_{min} = 298 K) in all simulations; thus, the cooling rate varies with ΔT and the process time.

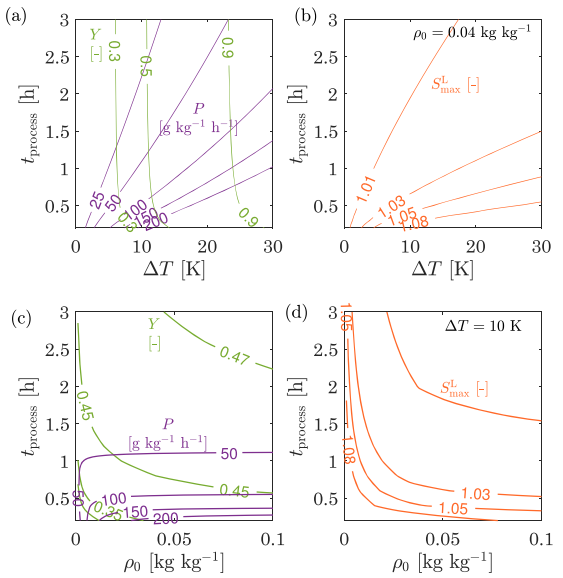

Figure 2. Effect of operating parameters (a, b) temperature range and process time (simulation 1) and (c, d) initial suspension density and process time (simulations 2) on the productivity (purple contour lines), on the yield (green contour lines), and on the maximum supersaturation of the undesired enantiomer, S^L_{max} (orange contour lines), when linear cooling is utilized (compound A).

Figure 2a shows that both the productivity and yield increase quickly with increasing temperature range, as a larger ΔT corresponds to faster cooling rates at a given process time. For the same reason, S^L_{max} (i.e., the probability of the extent of nucleation of the distomer) increases with increasing ΔT (Figure 2b), thus indicating that a tradeoff exists between high productivity and low distomer supersaturation. The cooling rate is also increased by decreasing $t_{process}$ (moving vertically from the top to the bottom in Figure 2a and b), which leads not only to higher productivity but also to larger distomer supersaturation, as expected.

Figure 2c and d (bottom row) shows the same KPIs in the ρ_0−$t_{process}$ parameter plane. Once again, the productivity and maximum supersaturation of the distomer increase with decreasing $t_{process}$, while the yield decreases due to an

https://doi.org/10.1021/acs.cgd.1c01374
Cryst. Growth Des. 2022, 22, 1427−1436

incomplete depletion of the supersaturation by growth. When looking at how the KPIs vary as a function of ρ_0 (i.e., moving horizontally in the plane), one notices a stronger effect at low values of suspension density, since the supersaturation builds up due to the small surface area available for growth. With increasing ρ_0, and thus increasing surface area, both productivity and maximum distomer supersaturation approach a constant value (Figure 2c and d). In contrast, the yield tends to increase with increasing initial suspension density (Figure 2c) and can be tuned not only with the choice of ρ_0 and $t_{process}$ but also via the selection of ΔT, which has a stronger effect on this quantity (see Figure 2a).

In conclusion, we observed that large temperature variations, long process times, and large initial suspension densities are beneficial for a high yield, by providing ideal conditions for consuming the supersaturation. Moreover, a clear tradeoff exists, as a function of ρ_0, $t_{process}$, and ΔT, between achieving either high productivity or low S^L_{max} (thus high purity) and high yield.

4.2. Mullin−Nyvlt-Based Cooling Profile for Increased Performance. CID has been performed with both linear and Mullin−Nyvlt-based cooling to compare their performance (simulation 3). For both cooling policies, the temperature range and initial suspension density are fixed and the process time needs to be selected. While the effect of these operating conditions with a linear cooling ramp is discussed in detail in section 4.1, the reader is referred to Appendix A for the results dedicated to the Mullin−Nyvlt-based cooling policy.

In this section, we compare the two cooling approaches by simulating the process with compound B, characterized by slow racemization kinetics and a shallow solubility curve, and with compound C, with fast racemization kinetics and a steep solubility curve. For both cooling methods and compounds, Figure 3 illustrates the tradeoff between the productivity and the yield (solid black and gray lines represent linear and Mullin−Nyvlt-based cooling, respectively, left axis), as well as the risk of nucleating the counter enantiomer (S^L_{max}, dashed light and dark blue lines represent linear and Mullin−Nyvlt-based cooling, respectively, right axis).

When the racemization is slow (Figure 3a, compound B), P decreases while Y increases with increasing $t_{process}$ (ρ_0, ΔT constant) for both cooling methods. The P−Y curves indicate that better performance is attained with the linear cooling profile: i.e., the Pareto curve is shifted to higher values and the KPIs are higher for given process times (Figure 3, points A and B). As discussed in section 4.1, a high P corresponds to a high S^L_{max}, thus limiting the purity and consequently the P value that is achievable in practice.

In the extreme case of infinitely fast racemization, larger productivity and yield are attained with the Mullin−Nyvlt-based cooling than with linear cooling. At the same time, the risk of undesired nucleation, S^L_{max}, under all conditions investigated is lower when the Mullin−Nyvlt-based cooling strategy is applied (Figure 3b, compound C). It is worth noting that, in this case, the productivity first increases with process time; as the crystallized mass becomes larger, then it decreases, as the increase in the crystal mass does not compensate for the longer process time. It follows that a maximum can be identified.

Note that large P−Y values can be achieved when the solubility curve is steep (compound C) and, depending on the system properties, different intermediate situations showing similar trends can be found, such in the case of compound A,

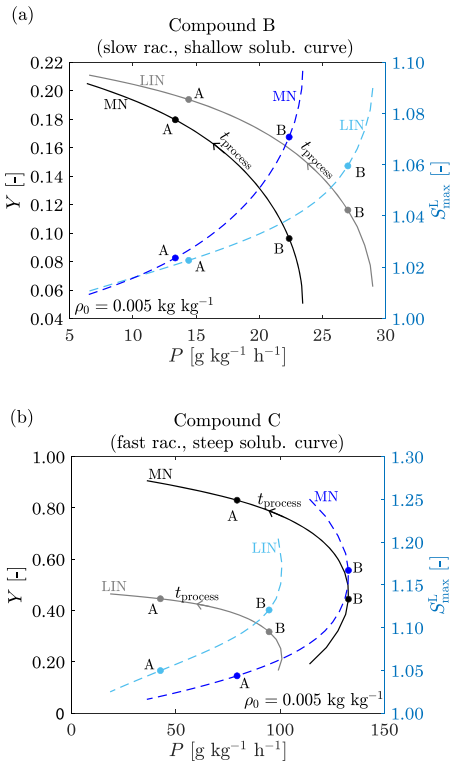

Figure 3. Comparison between the linear and the Mullin−Nyvlt cooling profiles for two simulated compounds with increasing rates of racemization and different solubilities (compounds B (a) and C (b), in this order, simulation 3): effect of varying $t_{process}$ at a constant suspension density and temperature range. The achievable P−Y levels (left axis, solid gray and black lines for linear and Mullin−Nyvlt-based cooling, respectively) and the corresponding S^L_{max} values (dashed light and dark blue lines for linear and Mullin−Nyvlt-based cooling, respectively) are reported. The arrows indicate increasing process times, while KPI values at two selected process times are highlighted by points A and B.

which is not discussed here for the sake of brevity. From these results, we conclude that utilizing the Mullin−Nyvlt-based profile instead of linear cooling can be beneficial for quickly racemizing systems, as in these cases the former allows reaching higher purity, productivity, and yield in comparison to the latter.

5. EXPERIMENTAL INVESTIGATION

In this section, we present the results of crystallization-induced deracemization experiments, where we investigate the effect of different operating parameters on the process outcome to verify and confirm the results obtained in the simulation study. First, we evaluate the effect of the seed loading (or suspension density) and of the cooling time, when a linear cooling profile is applied (LIN in Table 4). Then, we present two types of temperature profiles to improve the product purity. The first consists of applying the nonlinear temperature profile, i.e. Mullin−Nyvlt-based cooling (M-N in Table 4), presented in section 2.1; the second consists of partially dissolving the seeds before the cooling phase starts (PD in Table 4).

We chose a temperature range already tested for the deracemization via temperature cycles at the same scale for comparison (TC01 in Table 4): i.e. between 30 and 41 °C. The experimental conditions with the corresponding final purities (ee_{final}), productivities, and yields are reported in Table

https://doi.org/10.1021/acs.cgd.1c01374
Cryst. Growth Des. 2022, 22, 1427−1436

Table 4. Experimental Conditions and Results of Crystallization-Induced Deracemization Experiments with Reference to a Temperature Cycle Experiment (TC01)[a]

expt	TP	R_c (K min^{-1})	ρ_0	c_{DBU} (μL g^{-1})	ee_0	ee_{final}	P (g kg^{-1}h^{-1})	$t_{process}$ (h)	Y
TC01	TC	1.29	0.025	2.8	0.2	0.97 ± 0.01	0.88 ± 0.06	10.8 ± 0.8	
1	LIN	0.37	0.005	2.8	0.96	0.84 ± 0.04	6.9 ± 0.3	0.5	0.18 ± 0.02
2	LIN	0.09	0.005	2.8	0.94	0.84 ± 0.01	2.88 ± 0.01	2	0.27 ± 0.01
3	LIN	0.06	0.005	2.8	0.97	0.90	2.21	3	0.25
4	LIN	0.09	0.01	2.8	0.96	0.90	3.25	2	0.27
5	M-N		0.005	2.8	0.98	0.92	2.61	1.75	0.17
6	M-N		0.01	2.8	0.99	0.97	3.36	2	0.24
7	PD	0.09	0.005	2.8	0.96 (0.93)[b]	0.98 ± 0.01	1.02 ± 0.03	6	0.23 ± 0.01
8	PD	0.09	0.005	1.4	0.97 (0.99)[b]	0.88	0.85	6	0.25
9	PD	0.09	0.005	2.8[c]	0.95 (0.99)	0.98	1.00	6	0.18

[a]The minimum and maximum temperatures are 30 and 41 °C, respectively, and the solvent volume used is 50 mL (ca. 40 g). [b]The ee obtained upon dissolution, ee_{diss}, is reported in parentheses. [c]Solution equilibrated with 1.4 μL g^{-1} DBU. The same amount is added before the cooling phase starts.

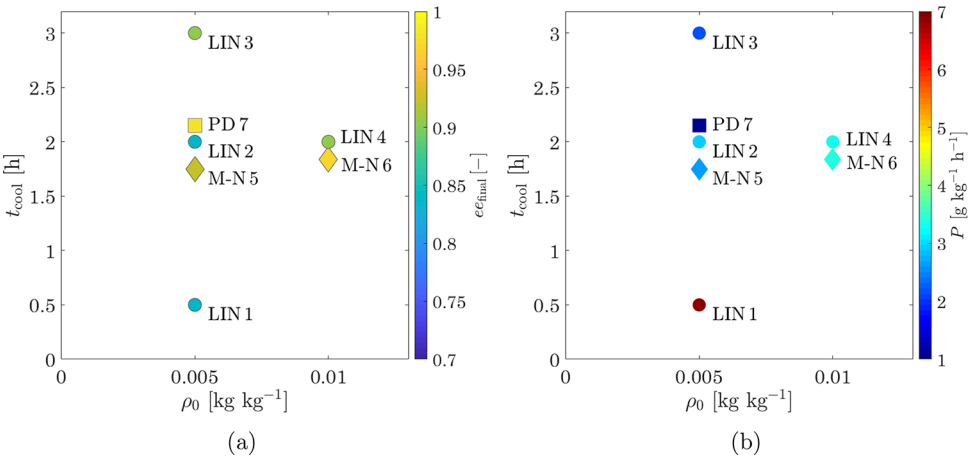

Figure 4. Purity (a) and productivity (b) as a function of seed loading and cooling time, for the experiments performed with linear (circles), Mullin−Nyvlt-based (diamonds), and PD (box symbol) cooling profiles. The last data points are plotted with slightly shifted coordinates for a better representation.

4. Some experiments were repeated twice (experiments 1, 2, and 7) in order to verify the reproducibility, which is indicated by the standard deviation from the mean value of the performance indicators in Table 4.

5.1. Effect of the Operating Conditions. The effect of the cooling time and of the seed loading is illustrated in Figure 4, where the purity and productivity are indicated for each data point by the symbol's color and the label indicates the corresponding experiment in Table 4, where the values of the yield are also reported.

By looking first at the experiments in which a linear cooling rate was applied (circles), we observe that the purity and the yield decrease when the cooling time is shortened, due to the higher supersaturation attained upon fast cooling (Table 4). In contrast, the productivity increases, because of the shorter process time, as expected and indicated by simulations. At a given cooling time and thus constant cooling rate, we observe that by increasing the seed loading, hence the surface area for crystal growth, higher purity can be attained with a slightly higher productivity and the same yield (experiment 2 vs experiment 4). Nevertheless, the final enantiomeric excess is still limited to 0.90, which is well below the desired target value.

5.2. Improving the Product Purity. To improve the purity of the product obtained with a linear cooling ramp, we propose here two different strategies: (i) applying the nonlinear profile, Mullin−Nyvlt based, presented in section 2.1 (Figure 1, black line), which can be designed as a function of only the solubility curve and the operating conditions; (ii) dissolving part of the seed mixture (Figure 1, green line) to eliminate the traces of the counter enantiomer present in the seeds that would grow upon cooling and would reduce the product purity.

5.2.1. Mullin−Nyvlt-Based Cooling Profile. From a comparison of the experiments where the linear (experiments 2 and 4) and the Mullin−Nyvlt-based profiles (experiments 5 and 6) are implemented, we conclude that, for a given operating point (or for a similar one, as in the case of experiments 2 and 5), better purity is achieved in the latter case (diamonds in Figure 4a), while the productivity variation is negligible (diamonds in Figure 4b) and the yield is lower for the former case (Table 4). Moreover, we observe that, for both types of cooling strategies, the ee_{final} and the productivity increase with increasing seed loading, but the yield improves only with the Mullin−Nyvlt-based profile. These data confirm the simulated trends but also show slight differences, which highlight the compound-specific behavior of the experimental system of interest.

It is worth noting that the Mullin−Nyvlt-based trajectory is based on specific assumptions, which are only approximately

https://doi.org/10.1021/acs.cgd.1c01374
Cryst. Growth Des. 2022, 22, 1427−1436

fulfilled in the case of the experimental compound, as the kinetics are not available. Nevertheless, because of its easy implementation and its better performance, the Mullin−Nyvlt-based trajectory for deracemization is recommended as an improvement with respect to simple linear cooling.

5.2.2. Partial Seed Dissolution. One of the critical aspects of CID is represented by the need for pure seed crystals to start the process. This material is obtained from previous purification processes that deliver a certain particle size distribution and purity, which might be lower than 100%. In this section we discuss how both these characteristics affect the process performance, thus highlighting the relevance of controlling the particle size of the seeding material. A way to get rid of the distomer impurities and to increase ee_0 before starting the cooling phase consists of dissolving part of the seed crystals, by increasing the temperature of the seeded solution by a few degrees, and starting the cooling ramp once the solution is re-equilibrated (Figure 1, green line).

This approach is tested at higher and lower catalyst concentrations, hence at higher and lower racemization rates, in experiments 7 and 8, respectively. Additionally, in experiment 9 the dissolution phase is performed at a low DBU concentration (1.4 μL g^{-1}), which is increased to twice that value (2.8 μL g^{-1}) before the cooling ramp starts. We observe that the ee increased upon heating when the catalyst concentration was low (experiments 8 and 9, Table 4), while it decreased from about 0.96 to 0.93 in experiment 7, which was repeated twice. This unexpected trend is attributed to a fast racemization reaction, which converts the eutomer into the distomer as soon as the former dissolves, thus hindering the dissolution of the latter and leading to the ee decrease. Nevertheless, the effect of the fast racemization rates is favorable during cooling and a high product purity, i.e. about 0.98, is attained in both experiments 7 and 9 (square in Figure 4a). In contrast, during cooling when the racemization rate is slow, the supersaturation of the counter enantiomer builds up and the final product purity is reduced by the nucleation and growth of the distomer (experiment 8). This highlights the relevance of the racemization rate, whose role is rationalized with the aid of the process model, as described in Appendix B.

On the basis of these experimental results, rationalized by the simulation study discussed in Appendix B, we conclude that, when the PD temperature profile is applied, the successful strategy is to avoid racemization during the dissolution step and to trigger the reaction only before cooling by adding the catalyst. By this approach the traces of the undesired enantiomer in the seeds can be eliminated, and the distomer nucleation upon cooling can be avoided, thus attaining higher product purity. When this approach is compared with the other two (LIN and M-N), the low productivity values (box symbol in Figure 4b and Table 4) resulting from the equilibration time needed after heating (4 h) represent a drawback of this technique. However, it should be noted that this holding time can be reduced on a case by case basis depending on the dissolution kinetics; for example if it is only 2 h, productivity values of up to 1.3−2 g kg^{-1} h^{-1} are obtained.

6. CONCLUSIONS

The modeling and experimental analysis carried out in this work has showed that the batch-crystallization-induced deracemization process is a simple and promising alternative to the deracemization via temperature cycles technique. However, the trends obtained from simulation results, confirmed by experimental studies, show a clear tradeoff between productivity and purity: high productivity can be achieved, but to cope with the possible initial presence and with the possible nucleation of the distomer, a careful selection of the operating conditions is necessary, as suggested in this work by the different strategies proposed. Moreover, the yield is large under operating conditions resulting in low productivity, as the former KPI benefits from long crystallization times to convert the enantiomer from the liquid phase to crystals, while the latter can profit from short process times.

On this basis, we conclude that, depending on the system of interest, either crystallization-induced deracemization or solid-state deracemization via temperature cycles can be the most convenient process. On the one hand, deracemization via temperature cycles guarantees the attainment of high product purity; however, productivity values are generally low (only 0.88 g kg^{-1} h^{-1} for NMPA; see Table 4), because they are limited by the initial suspension density. Nevertheless, this method is attractive either when nucleation of the counter enantiomer cannot be avoided or when crystals with high enantiomeric excess need to be produced: e.g., to be utilized as a starting material for further processing. On the other hand, crystallization-induced deracemization is simple to implement and to scale up because of its analogy with cooling crystallization processes (e.g., preferential crystallization). However, its productivity strongly depends on solubility and high product purity can be attained only if it is possible to avoid distomer nucleation. To this aim, four effective strategies were proposed in this work: increasing the seed loading, utilizing the Mullin−Nyvlt-based cooling profile, optimizing the catalyst concentration level, and partially dissolving the seeds. Note that the cooling ramp could be followed by two finishing procedures. The first involves performing a couple of temperature cycles to convert the distomer traces into the eutomer, thus increasing the final enantiomeric excess. The second consists of keeping the suspension at constant temperature to improve the process yield, provided that the product purity is not affected.

Through this study on crystallization-induced deracemization, which follows our previous work on deracemization via temperature cycles,[10,11,15,16,18,21] we have completed the analysis of a class of deracemization processes operated batchwise. We have proven that such batch processes are effective, also due to the simplicity of their operation, and we have highlighted their advantages and disadvantages in terms of key performance indicators. It is worth noting that an alternative approach is offered by continuous processes, which can in principle achieve a higher level of operational stability and of product quality consistency. How to realize a continuous deracemization process based on the same physicochemical mechanisms exploited in this study and how this compares in terms of process performance are beyond the scope of this work and are the subjects of an upcoming contribution.[31]

APPENDICES

In this section, two model-based investigations are presented to shed light on further aspects of deracemization by cooling. The details on how the Mullin−Nyvlt-based cooling profile can improve the process performance with respect to linear cooling is described in Appendix A. Appendix B investigates with simulations the evolution of the enantiomeric excess to clarify the trends observed in partial dissolution experiments.

https://doi.org/10.1021/acs.cgd.1c01374
Cryst. Growth Des. 2022, 22, 1427−1436

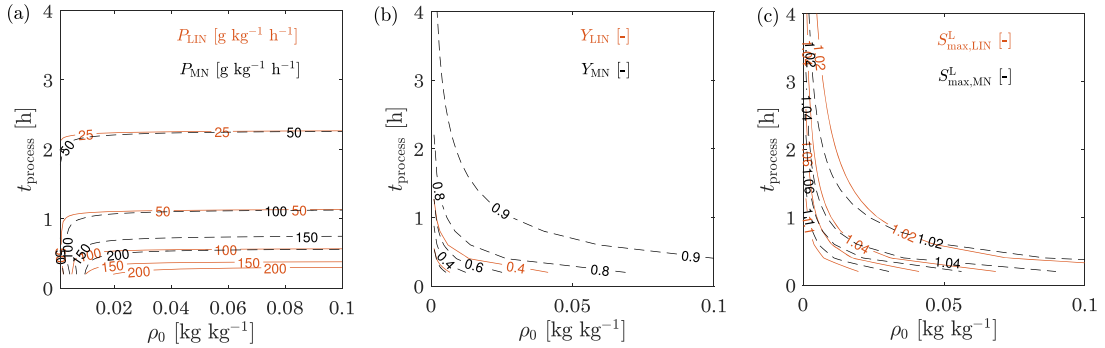

Figure 5. Effect of initial suspension density and process time (a) on the productivity, (b) on the yield, and (c) on the maximum supersaturation of the undesired enantiomer when linear (orange solid contour lines) and Mullin−Nyvlt-based cooling profiles (black dashed contour lines) are applied (compound C).

Then, the derivation of the Mullin−Nyvlt-based trajectory is provided in Appendix C.

APPENDIX A: DETAILED COMPARISON OF THE COOLING PROFILES

To highlight the difference between the linear and the Mullin−Nyvlt-based cooling profile, we focus on the case of compound C, as the difference between the two cooling policies is the most striking for this compound. In Figure 5a,b, the productivity and yield are presented with orange solid lines and dashed black lines for linear and Mullin−Nyvlt-based cooling, respectively. The trends are similar to that obtained with linear cooling: namely, the productivity is large by utilizing fast cooling rates with large initial suspension density and the yield increases with increasing process time. Moreover, for a given operating point, the two cooling policies lead to a substantial difference in the KPI values, as indicated by the labels of the contour lines plotted for each case at the same levels, and the application of the Mullin−Nyvlt-based cooling enables achieving larger productivity and yield in comparison to the linear cooling. For both cooling policies, S^L_{max} is larger and thus a higher risk of nucleation is expected on operating with a small amount of seed and at short process times, as shown by Figure 5c. However, the contour line corresponding to S^L_{max} = 1.02 shifts to the left when the Mullin−Nyvlt-based cooling is applied (dashed black contour lines), thus indicating that a lower S^L_{max} is reached under the given operating conditions with this temperature profile. The latter cooling strategy is shown to outperform the former in terms of S^L_{max} under a wide range of operating conditions.

APPENDIX B: VARIATION OF ENANTIOMERIC EXCESS AFTER PARTIAL DISSOLUTION

To improve the understanding of the experimental results obtained when partial seed dissolution is performed (section 5.2.2), we exploited the process model presented in section 2.3 to simulate a simple dissolution phase, which is a heating ramp (R_h = 0.033 K s^{-1}) from the starting temperature, i.e. T_{min}= 312 K, to the maximum temperature, i.e. T_{max}= 314 K, followed by an equilibration period at this temperature (14400 s, t_r = 30720 s; for the values of the other parameters see Table 2).

It is known from previous studies that deracemization processes are sensitive to the initial conditions,[10,32] such as the mass and size of the crystals of each enantiomer, and to the system kinetic properties,[16,18] i.e. racemization, dissolution, and growth rates. The interplay among these parameters determines how the supersaturation of the two enantiomers in solution varies and, hence, the driving force that each enantiomer experiences as it dissolves. Therefore, we have exploited the process model to clarify the experimental trends during the dissolution phase and their dependence on the process and system parameters, by selecting two of them: (i) the racemization rate constant $k_{r,0}$ and (ii) the initial mean size ratio of the particles of the two enantiomers $L_{D,0}/L_{L,0}$, where $L_{D,0}$ is set to 50 μm ($\sigma_{D,0} = \sigma_{L,0}$ = 0.05 μm) and $L_{L,0}$ is modified accordingly. Considering that the seeds used in the experiments were produced through deracemization via temperature cycles, we varied the particle size, on the basis of the results of a set of 260 simulations, where in 3 out of 4 cases $L_{D,0}$ (eutomer) is larger than $L_{L,0}$ (distomer), while the opposite happens in the other case (1 out of 4).

For different combinations of the selected variables, Figure 6 illustrates how the ee of an enantiomerically enriched mixture

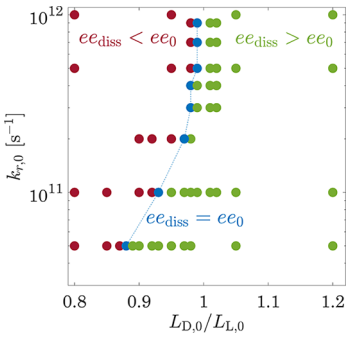

Figure 6. Effect of the initial ratio of mean particle sizes and racemization rate on the ee resulting in simulations where a suspension with ρ_0 = 0.014, ee_0 = 0.96, and $L_{D,0}$ = 50 μm is heated from 39 to 41 °C.

(ee_0 = 0.96) can vary upon heating and partial dissolution. For slow racemization rates, the ee increases upon heating (green circles), unless the size asymmetry between the two populations is large. Specifically, this is the case when the distomer particles are too big to dissolve ($L_{L,0} > L_{D,0}$); thus, the eutomer dissolution is promoted. However, when the racemization rate becomes faster, smaller differences in the mean size of the two enantiomers can be crucial to determine the decrease (red circles) or increase (green circles) of the enantiomeric excess upon heating and partial dissolution. Note that, as several parameters influence the process, the threshold

https://doi.org/10.1021/acs.cgd.1c01374
Cryst. Growth Des. 2022, 22, 1427−1436

(blue dashed line connecting the blue circles, i.e. $ee_{diss} = ee_0$) determining how the ee varies will change position in the plane in Figure 6, when other conditions, such as the seed loading and the dissolution rate, vary, but the qualitative picture and the associated behavior will not.

APPENDIX C: DERIVATION OF THE MULLIN–NYVLT-BASED TRAJECTORY FOR DERACEMIZATION BY COOLING

The mass balance equations of both enantiomers can be written together with the equation describing the third moment as a function of time as

$$c_D' = -\rho_c k_v m_3' + K(c_L - c_D) \tag{16a}$$

$$c_L' = K(c_D - c_L) \tag{16b}$$

$$\text{with } m_3(t) = \frac{m_s}{\rho_c k_v L_s^3}(L_s + Gt)^3 \tag{16c}$$

Note that eq 16c has been formulated assuming constant growth rate and monodisperse seeds with size L_s. The corresponding initial conditions are

$$c_D(t=0) = c_0^D$$

$$c_L(t=0) = c_0^L$$

$$m_s = \rho_c k_v m_3(0) = \rho_c k_v n_0 L_s^3 \tag{17}$$

By summing up eqs 16a and 16b, we obtain

$$(c_D + c_L)' = -\rho_c k_v m_3' \tag{18}$$

We define the total concentration as $c_{tot}(t) = c_D + c_L$, and integration over time results in

$$c_{tot}(t) = c_0^{tot} - \rho_c k_v m_3(t) + m_s = c_0^{tot} - m_s\left(\left(1 + \frac{Gt}{L_s}\right)^3 - 1\right) \tag{19}$$

Similarly, the final concentration can be expressed as

$$c_{final}^{tot} = c_0^{tot} - m_s\left(\left(1 + \frac{Gt_0}{L_s}\right)^3 - 1\right) \tag{20}$$

After c_{final}^{tot} is subtracted from eq 19 and divided by $c_0^{tot} - c_{final}^{tot}$, this results in

$$\frac{c_{tot}(t) - c_{final}^{tot}}{c_0^{tot} - c_{final}^{tot}} = \frac{c_0^{tot} - c_{final}^{tot}}{c_0^{tot} - c_{final}^{tot}} - \frac{m_s\left(\left(1 + \frac{Gt}{L_s}\right)^3 - 1\right)}{m_s\left(\left(1 + \frac{Gt_0}{L_s}\right)^3 - 1\right)} \tag{21}$$

By defining the following rescaled quantities

$$\hat{c}(\tau) = \frac{c_{tot} - c_{final}^{tot}}{c_0^{tot} - c_{final}^{tot}} \quad \tau = \frac{t}{t_0} \quad \alpha = \frac{Gt_0}{L_s} \tag{22}$$

one obtains

$$\hat{c}(\tau) = 1 - \frac{(1 + \alpha\tau)^3 - 1}{(1 + \alpha)^3 - 1} \tag{23}$$

After some algebraic modification of eq 20, the following relation can be derived:

$$\frac{Gt_{final}}{L_s} = \left(\frac{c_0^{tot} - c_{final}^{tot}}{m_s} + 1\right)^{1/3} - 1 \tag{24}$$

Then, by defining the dimensionless mass $\mu_s = \frac{m_s}{c_0^{tot} - c_{final}^{tot}}$, a simple expression for α can be obtained:

$$\alpha = \left(\frac{1}{\mu_s} + 1\right)^{1/3} - 1 \tag{25}$$

Finally, the saturation trajectory (i.e., eq 23) can be converted into the temperature trajectory using the solubility, $c_\infty = q_0 \exp\left(-\frac{q_1}{T}\right)$, to get the final equation, i.e. eq 1, for the temperature profile.

AUTHOR INFORMATION

Corresponding Author

Marco Mazzotti − *Institute of Energy and Process Engineering, ETH Zurich, 8092 Zurich, Switzerland;* orcid.org/0000-0002-4948-6705; Phone: +41 44 632 24 56; Email: marco.mazzotti@ipe.mavt.ethz.ch; Fax: +41 44 632 11 41

Authors

Brigitta Bodák − *Institute of Energy and Process Engineering, ETH Zurich, 8092 Zurich, Switzerland;* orcid.org/0000-0002-1979-9815

Francesca Breveglieri − *Institute of Energy and Process Engineering, ETH Zurich, 8092 Zurich, Switzerland;* orcid.org/0000-0002-0034-7966

Complete contact information is available at: https://pubs.acs.org/10.1021/acs.cgd.1c01374

Author Contributions

†B.B. and F.B. contributed equally to this work and have been entered in alphabetical order.

Notes

The authors declare no competing financial interest.

ACKNOWLEDGMENTS

The authors thank Fabia Arpago for accurate experimental investigations carried out for this work. This research received funding as part of the CORE Project (October 2016-December 2020) from the European Union's Horizon 2020 Research and Innovation Program under Marie Sklodowska-Curie Grant Agreement 722456 CORE ITN and also from the European Research Council (ERC) under the European Unions Horizon 2020 Research and Innovation Programme under Grant Agreement No. 788607.

REFERENCES

(1) Viedma, C. Chiral Symmetry Breaking During Crystallization: Complete Chiral Purity Induced by Nonlinear Autocatalysis and Recycling. *Phys. Rev. Lett.* **2005**, *94*, 065504.

(2) Noorduin, W. L.; Meekes, H.; Van Enckevort, W. J.; Millemaggi, A.; Leeman, M.; Kaptein, B.; Kellogg, R. M.; Vlieg, E. Complete deracemization by attrition-enhanced Ostwald ripening elucidated. *Angew. Chemie - Int. Ed.* **2008**, *47*, 6445−6447.

(3) Noorduin, W. L.; van der Asdonk, P.; Bode, A. A. C.; Meekes, H.; van Enckevort, W. J. P.; Vlieg, E.; Kaptein, B.; van der Meijden,

https://doi.org/10.1021/acs.cgd.1c01374
Cryst. Growth Des. 2022, 22, 1427−1436

M. W.; Kellogg, R. M.; Deroover, G. Scaling Up Attrition-Enhanced Deracemization by Use of an Industrial Bead Mill in a Route to Clopidogrel (Plavix). *Org. Process Res. Dev.* **2010**, *14*, 908−911.
(4) Iggland, M.; Mazzotti, M. A Population Balance Model for Chiral Resolution via Viedma Ripening. *Cryst. Growth Des.* **2011**, *11*, 4611−4622.
(5) Suwannasang, K.; Flood, A. E.; Rougeot, C.; Coquerel, G. Using Programmed Heating-Cooling Cycles with Racemization in Solution for Complete Symmetry Breaking of a Conglomerate Forming System. *Cryst. Growth Des.* **2013**, *13*, 3498−3504.
(6) Iggland, M.; Fernández-Ronco, M. P.; Senn, R.; Kluge, J.; Mazzotti, M. Complete solid state deracemization by High Pressure Homogenization. *Chem. Eng. Sci.* **2014**, *111*, 106−111.
(7) Xiouras, C.; Van Aeken, J.; Panis, J.; Ter Horst, J. H.; Van Gerven, T.; Stefanidis, G. D. Attrition-Enhanced Deracemization of NaClO3: Comparison between Ultrasonic and Abrasive Grinding. *Cryst. Growth Des.* **2015**, *15*, 5476−5484.
(8) Suwannasang, K.; Flood, A. E.; Rougeot, C.; Coquerel, G. Use of Programmed Damped Temperature Cycles for the Deracemization of a Racemic Suspension of a Conglomerate Forming System. *Org. Process Res. Dev.* **2017**, *21*, 623−630.
(9) Li, W. W.; Spix, L.; De Reus, S. C.; Meekes, H.; Kramer, H. J.; Vlieg, E.; Ter Horst, J. H. Deracemization of a racemic compound via its conglomerate-forming salt using temperature cycling. *Cryst. Growth and Des.* **2016**, *16*, 5563−5570.
(10) Bodák, B.; Maggioni, G. M.; Mazzotti, M. Population-Based Mathematical Model of Solid-State Deracemization via Temperature Cycles. *Cryst. Growth Des.* **2018**, *18*, 7122−7131.
(11) Breveglieri, F.; Maggioni, G. M.; Mazzotti, M. Deracemization of NMPA via Temperature Cycles. *Cryst. Growth Des.* **2018**, *18*, 1873−1881.
(12) Belletti, G.; Meekes, H.; Rutjes, F. P. J. T.; Vlieg, E. Role of Additives during Deracemization Using Temperature Cycling. *Cryst. Growth Des.* **2018**, *18*, 6617−6620.
(13) Cameli, F.; Xiouras, C.; Stefanidis, G. D. Intensified deracemization via rapid microwave-assisted temperature cycling. *CrystEngComm* **2018**, *20*, 2897−2901.
(14) Steendam, R. R. E.; ter Horst, J. H. Scaling Up Temperature Cycling-Induced Deracemization by Suppressing Nonstereoselective Processes. *Cryst. Growth Des.* **2018**, *18*, 3008−3015.
(15) Bodák, B.; Maggioni, G. M.; Mazzotti, M. Effect of Initial Conditions on Solid-State Deracemization via Temperature Cycles: A Model-Based Study. *Cryst. Growth Des.* **2019**, *19*, 6552−6559.
(16) Breveglieri, F.; Mazzotti, M. Role of Racemization Kinetics in the Deracemization Process via Temperature Cycles. *Cryst. Growth Des.* **2019**, *19*, 3551−3558.
(17) Oketani, R.; Hoquante, M.; Brandel, C.; Cardinael, P.; Coquerel, G. Resolution of an Atropisomeric Naphthamide by Second-Order Asymmetric Transformation: A Highly Productive Technique. *Org. Process Res. Dev.* **2019**, *23*, 1197−1203.
(18) Breveglieri, F.; Baglai, I.; Leeman, M.; Noorduin, W. L.; Kellogg, R. M.; Mazzotti, M. Performance Analysis and Model-Free Design of Deracemization via Temperature Cycles. *Org. Process Res. Dev.* **2020**, *24*, 1515−1522.
(19) Intaraboonrod, K.; Harriehausen, I.; Carneiro, T.; Seidel-Morgenstern, A.; Lorenz, H.; Flood, A. E. Temperature Cycling Induced Deracemization of DL-Asparagine Monohydrate with Immobilized Amino Acid Racemase. *Cryst. Growth Des.* **2021**, *21*, 306.
(20) Cameli, F.; ter Horst, J. H.; Steendam, R. R.; Xiouras, C.; Stefanidis, G. D. On the Effect of Secondary Nucleation on Deracemization through Temperature Cycles. *Chem.-Eur. J.* **2020**, *26*, 1344−1354.
(21) Breveglieri, F.; Bodák, B.; Mazzotti, M. Deracemization via periodic and non-periodic temperature cycles: rationalization and experimental validation of a simplified process design approach. *Org. Process Res. Dev.* **2021**, *25*, 2551−2565.
(22) Anderson, N. G. Developing processes for crystallization-induced asymmetric transformation. *Org. Process Res. Dev.* **2005**, *9*, 800−813.
(23) Fogassy, E.; Nógrádi, M.; Kozma, D.; Egri, G.; Pálovics, E.; Kiss, V. Optical resolution methods. *Org. Biomol. Chem.* **2006**, *4*, 3011−3030.
(24) Levilain, G.; Rougeot, C.; Guillen, F.; Plaquevent, J. C.; Coquerel, G. Attrition-enhanced preferential crystallization combined with racemization leading to redissolution of the antipode nuclei. *Tetrahedron Asymmetry* **2009**, *20*, 2769−2771.
(25) Oketani, R.; Marin, F.; Tinnemans, P.; Hoquante, M.; Laurent, A.; Brandel, C.; Cardinael, P.; Meekes, H.; Vlieg, E.; Geerts, Y.; Coquerel, G. Deracemization in a Complex Quaternary System with a Second-Order Asymmetric Transformation by Using Phase Diagram Studies. *Chem.-Eur. J.* **2019**, *25*, 13890−13898.
(26) Bodák, B.; Breveglieri, F.; Mazzotti, M. On the model-based design and comparison of crystallization-based deracemization techniques. Manuscript in preparation.
(27) Mullin, J.; Nývlt, J. Programmed cooling of batch crystallizers. *Chem. Eng. Sci.* **1971**, *26*, 369−377.
(28) Ward, J. D.; Yu, C.-C.; Doherty, M. F. A new framework and a simpler method for the development of batch crystallization recipes. *AIChE J.* **2011**, *57*, 606−617.
(29) Mullin, J. *Crystallization*, 4th ed.; Butterworth-Heinemann Press: Oxford, U.K., 2001.
(30) Gou, L.; Lorenz, H.; Seidel-Morgenstern, A. Investigation of a chiral additive used in preferential crystallization. *Cryst. Growth Des.* **2012**, *12*, 5197−5202.
(31) Bodák, B.; Mazzotti, M. Solid-State Deracemization via Temperature Cycles in Continuous Operation: A Model-based Process Design. Submitted for publication.
(32) Iggland, M.; Müller, R.; Mazzotti, M. On the Effect of Initial Conditions in Viedma Ripening. *Cryst. Growth Des.* **2014**, *14*, 2488−2493.

https://doi.org/10.1021/acs.cgd.1c01374
Cryst. Growth Des. 2022, 22, 1427−1436